

# The importance of specific heat characterization when reporting new superconductors and superconductivity in LiGa<sub>2</sub>Rh

Elizabeth M. Carnicom<sup>1</sup>, Weiwei Xie<sup>2</sup>, Zoe Yang<sup>1</sup>, Karolina Górnicka<sup>3</sup>, Tai Kong<sup>1</sup>, Tomasz Klimczuk<sup>3</sup>, and R. J. Cava<sup>1</sup>

<sup>1</sup>*Department of Chemistry, Princeton University, Princeton, New Jersey 08544*

<sup>2</sup>*Department of Chemistry, Louisiana State University, Baton Rouge LA 70803*

<sup>3</sup>*Department of Physics, Gdansk University of Technology, Gdansk Poland 80-233*

## Abstract

We show that the crystallographically ordered full Heusler compound LiGa<sub>2</sub>Rh is a superconductor with  $T_c = 2.4$  K. The new superconductor was found as a result of an intuition-based extension of a database search for superconductors that looked for the presence of peaks in the electronic band structure near the Fermi Energy. Measurement of the entropy loss during the transition from the non-superconducting to the superconducting state, a straightforward measurement rarely presented in reports of “new” superconducting materials, played a critical role in identifying and isolating the superconducting compound. This study presents a particularly good example of how specific heat measurements are important for the identification and isolation of a new superconductor, since much more frequently reported resistive and magnetic susceptibility characterization are often not enough to confirm the identification of a new superconducting material.

## Introduction

Heusler compounds, first discovered in 1903 by Friedrich Heusler,<sup>1</sup> remain active subjects of research more than a century later with over 1,000 reported compounds in the family.<sup>2</sup> Heusler compounds are ternary intermetallic materials that exist in either a 1:1:1 or a 2:1:1 elemental ratio with the general formulas  $XYZ$  (half-Heusler) or  $X_2YZ$  (full-Heusler), where  $X$  and  $Y$  are typically transition metals and  $Z$  is typically a main group element. In some Heusler compounds,  $Y$  can be a rare earth element<sup>3</sup>, alkaline earth element<sup>4</sup>, or alkali metal<sup>5</sup> and  $X$  can sometimes be a main group element. (The formulas of Heusler compounds are typically presented with the atoms in order of increasing electronegativity, or with  $X$  presented first. The possible formulas of our Heusler are  $\text{Ga}_2\text{LiRh}$ ,  $\text{LiGa}_2\text{Rh}$ , or  $\text{LiRhGa}_2$ . Even though the crystal structure of this Heusler was originally reported with the formula  $\text{LiRhGa}_2$ ,<sup>6</sup> here we employ the formula style  $\text{LiGa}_2\text{Rh}$  to be consistent with other reported Heusler superconductors, which have the  $X_2$  atom written second<sup>7</sup>.) Full-Heusler compounds crystallize with the  $L2_1$  structure (space group  $Fm-3m$ , No. 225) and contain atoms that are ordered on the  $4a$  (0, 0, 0),  $8c$  ( $\frac{1}{4}$ ,  $\frac{1}{4}$ ,  $\frac{1}{4}$ ) and  $4b$  ( $\frac{1}{2}$ ,  $\frac{1}{2}$ ,  $\frac{1}{2}$ ) Wyckoff positions, yielding the 1:2:1 ratio, while half-Heusler compounds crystallize in the  $C1_b$  structure (space group  $F-43m$ , No. 216) with the atoms occupying the  $4a$ ,  $4b$ , and  $4c$  positions, yielding the 1:1:1 ratio. The crystal structure of a full-Heusler compound can be described as consisting of 4 interpenetrating  $fcc$  sublattices, all filled, with one of those  $fcc$  sublattices unoccupied in the half-Heusler compounds.<sup>8</sup> In addition, inverse full Heusler compounds are also sometimes encountered, such as in  $\text{Mn}_2\text{CoSn}$ <sup>2,9</sup> or  $\text{Mn}_2\text{CoGa}$ <sup>10</sup> which both crystallize in the  $\text{CuHg}_2\text{Ti}$  structure-type where the  $X$  atoms no longer form a simple cubic lattice and are positioned on both the  $4a$  and  $4d$  Wyckoff positions. Furthermore, Heusler phases need not be stoichiometric or fully ordered as is seen in  $\text{Co}_2\text{FeAl}$ <sup>11</sup> and  $\text{Co}_{1+x}\text{Fe}_{2-x}\text{Si}$ <sup>12</sup>, for example. The variety of compounds seen in the Heusler family

can be thought of as an intermetallic analogy to the more frequently encountered normal and inverse, and partially inverse spinels.

These materials<sup>2,8,13</sup> have been studied not only for spintronic device applications<sup>14,15</sup> but also because they host a wide range of interesting physical phenomena such as heavy fermion behavior<sup>16–19</sup>, thermoelectric properties<sup>20–22</sup>, semi-conducting behavior<sup>23,24</sup>, ferromagnetism<sup>25–30</sup>, and superconductivity<sup>3,7,31–37</sup>.  $\text{Cu}_2\text{MnAl}$ , for example, the first discovered Heusler, orders ferromagnetically even though it does not contain any ferromagnetic elements<sup>1</sup> and  $\text{Co}_2\text{FeSi}$  has the highest magnetic moment and Curie temperature in reported Heusler compounds.<sup>27,28</sup> Of the plethora of Heusler compounds known to exist, only a small percentage (~3 %) are reported superconductors. Some of the first Heusler superconductors discovered were the Pd-based compounds  $A\text{Pd}_2\text{Sn}$  ( $A = \text{Y, Lu, Sc}$ ).<sup>3,38,39</sup> In addition,  $\text{ErPd}_2\text{Sn}$ <sup>35</sup> and  $\text{YbPd}_2\text{Sn}$ <sup>32</sup> are both full-Heusler compounds that display evidence for the coexistence of superconductivity and magnetic ordering. Some Heusler superconductors with Ga as the main group element are  $\text{ZrNi}_2\text{Ga}$  ( $T_c = 2.9 \text{ K}$ )<sup>36</sup>,  $\text{HfNi}_2\text{Ga}$  ( $T_c = 1.12 \text{ K}$ )<sup>31</sup>, and  $\text{NbNi}_2\text{Ga}$  ( $T_c = 1.54 \text{ K}$ )<sup>34</sup>. All these superconductors contain transition metals as the  $X_2$  atoms in the full-Heusler formula  $YX_2Z$ . A handful of half-Heusler superconductors have also been reported.<sup>40–44</sup> To the best of our knowledge, there are no previously reported full-Heusler superconductors containing lithium. The reported Heusler superconductors satisfy Matthias' rules for superconductivity in transition metal compounds, with the best superconductors found for the number of valence electrons per atom falling in the range between 6 and 8.<sup>45,46</sup> The Heusler superconductor reported in this work still satisfies Matthias' rules, but is at the onset of the first “peak” in expected superconducting behavior, with only 4 valence electrons per atom.

When testing for superconductivity, there are typically three main measurements used: magnetic susceptibility, electrical resistivity, and heat capacity. Resistivity and magnetic susceptibility are highly sensitive techniques that can show a superconducting transition when even a small percentage of superconductor is present. With those measurements in hand, then only heat capacity can truly confirm if a material is a bulk superconductor. When a superconducting material is cooled below its critical temperature,  $T_c$ , its electrons undergo a transition from the normal state to the superconducting state. In the normal state, the electrons are disordered and therefore have a higher degree of entropy. When the material transitions to the superconducting state, the electrons enter an ordered state where the electrons pair up. Heat capacity allows for the direct measurement of the entropy loss at this transition, which, for conventional superconductors is represented by the normalized specific heat jump  $\Delta C/\gamma T_c = 1.43$ . This value was revealed by the BCS theory for weak coupling superconducting materials, and is found to be the case for the vast majority of superconductors.<sup>47</sup> By plotting the specific heat data as  $C_p/T$  vs.  $T$ , the jump in specific heat  $\Delta C$  at the transition temperature  $T_c$ , can then be divided by  $\gamma$ , the Sommerfeld parameter, a proportionality constant that is related to the electronic density of states, another quantity easily measured by specific heat. If the measured entropy loss is not near 1.43, then the observed superconductivity is most likely from a superconducting impurity in the sample and not actually from the bulk of the material, despite how pure the sample appears to be by X-ray diffraction or how strong the superconducting signal is by magnetic susceptibility.

Temperature-dependent specific heat measurements are important not only to confirm the purity of a superconducting sample but are also especially important when one or more of the impurities are superconducting. For example, superconductivity was reported in  $Ti_2InX$  ( $X = C, N$ )<sup>48,49</sup> and  $Nb_2SnC$ <sup>50</sup> using only magnetization and resistance measurements. However, in these

systems there are elemental superconductors such as In, Nb, and Sn known, in addition to binary superconductors such as NbC, InN, TiN, Nb<sub>3</sub>Sn, NbN, and various In-Sn compositions, to name a few. X-ray diffraction is often insensitive to very small percentages of impurities, and if those impurities are superconducting then there will still be an observed diamagnetic signal by magnetic susceptibility. In addition, the observed  $T_c$  can still be from a superconducting impurity even if the  $T_c$  is different from what has been previously reported for that impurity, since sample purity often affects  $T_c$ . While  $Ti_2InX$  ( $X = C, N$ ) and  $Nb_2SnC$  may very well be bulk superconductors, the claim that they are is not concrete without specific heat data, especially since there are so many potential superconducting impurities in these systems. In contrast, superconductivity in  $BaPb_3$ ,  $Ba_{0.89}Sr_{0.11}Pb_3$ , and  $Ba_{0.5}Sr_{0.5}Pb_3$ ,<sup>51</sup> which were all grown out of a Pb flux, has been reported with confirmation by specific heat measurements. Since Pb is an elemental superconductor, any small percentage of unreacted Pb would have resulted in a superconducting signal by magnetic susceptibility measurements and potentially zero resistance. Further, with the potential for superconductivity for many of the binary or ternary phases in this system, it was the specific heat measurements performed on the various samples that confirmed that the compounds  $BaPb_3$ ,  $Ba_{0.89}Sr_{0.11}Pb_3$ , and  $Ba_{0.5}Sr_{0.5}Pb_3$  are actually new superconductors.

Here we present the synthesis and characterization of a new superconducting material and stress the importance of using specific heat measurements when reporting new superconductors. Our superconductor was found through an extension of a Materials Project database<sup>52</sup> search for peaks in the electronic density of states near the Fermi Energy. These peaks are often due to the presence of van Hove singularities in the electronic structure, a characteristic frequently observed in superconducting materials, motivating the search.<sup>53-55</sup> The crystal structure of our previously unreported full-Heusler superconductor,  $LiGa_2Rh$ , was determined using single-crystal X-ray

diffraction and found to be fully crystallographically ordered. The superconductivity was characterized through temperature-dependent magnetic susceptibility, specific heat, and electrical resistivity ( $T_c = 2.4$  K) measurements. Field-dependent magnetization measurements were used to determine the lower critical magnetic field ( $H_{c1}$ ) and the specific heat measurements confirm that the observed superconducting transition is from the bulk of the Heusler material and is of the weak-coupling BCS type. The use of specific heat measurements for the identification and isolation of a new superconducting material is critical in all cases where there is the possibility of interference from other phases present. Characterization of pure and impure materials by SEM (Scanning electron microscopy) and EDS (Energy Dispersive X-ray Spectroscopy) elemental mapping is employed to demonstrate how the use of susceptibility measurements alone can be misleading. The case described here, where the powder X-ray diffraction patterns of  $\text{LiGa}_2\text{Rh}$  and the GaRh “impurity” phase are nearly coincident, is a particularly good example of the importance of entropy loss via specific heat measurements, but the general use of such measurements in the first reports of new superconductors would avoid many mistaken or ambiguous reports in the literature.

## **Experimental**

The initial search for potential new intermetallic superconductors was performed via a code designed to sift the calculated electronic structures found in the Materials Project data set to look for the presence of peaks in the electronic density of states within 0.25 eV of the Fermi energy. We note that a favorable electronic structure is not a sufficient condition for predicting superconductors, largely because it ignores the factors that couple the electronic system to the pairing force, which, for conventional superconductors such as the present one, are phonons. The presence of a peak in the electronic density of states in the vicinity of  $E_F$  is observed in many superconducting materials, and the magnitude of the electronic density of states is a significant

factor in the McMillan formula for  $T_c$  for conventional superconductors. The database screening suggested that the material  $\text{LiPd}_2\text{Ga}$  might be superconducting. Attempted synthesis of that material did not show evidence of superconductivity above 1.8 K. Replacement of Pd by Rh, a  $4d$  element sometimes encountered in superconducting intermetallic compounds, did yield a superconducting material. The superconductor was identified and isolated in pure form using a combination of X-ray diffraction analysis, magnetic susceptibility, specific heat, and resistivity measurements, as described below, and is the  $\text{LiGa}_2\text{Rh}$  full Heusler compound.

After identification of the superconducting phase, polycrystalline  $\text{LiGa}_2\text{Rh}$  was synthesized from the starting materials gallium (>99.99%, pellet, 6mm dia., Aldrich), rhodium (99.9%, bullion, Baird & Co. Bullion Merchants), and lithium (<99+ %, chunk, Alfa). A tantalum tube (6.35mm OD x 0.381 wall, Eagle Alloys) was crimped and arc-melted under Argon to seal one end. The rhodium and gallium metals were then added to the tantalum tube, which was then brought into a PureLab He argon-filled glove box. A fresh piece of lithium was cut to remove any oxide layer and was added to the Ta tube with the Ga and Rh. The resulting elemental ratios Li:Ga:Rh for the reaction were 1.02:2.05:1, employing 2% excess Li and 2.5 % excess Ga. The tube was then closed partway with pliers and transferred to a Materials Research Furnace arc-melter. The Ta tube was sealed under ~600 mbar Ar quickly to ensure that the contents of the tube would not get too hot and pre-react. The Ta tube was then sealed in a quartz tube under vacuum to ensure that the Ta tube would not oxidize during the heating cycle. The samples were then heated to 750 °C at a rate of 3 °C/min, held at 750 °C for 2.5 days and finally quenched to room temperature in air.

$\text{LiGa}_2\text{Rh}$ , although Li-containing, is stable in air over time and therefore was handled outside of the glovebox for all experiments; sample degradation was not observed. Following the

heating cycle, the sample of LiGa<sub>2</sub>Rh was mechanically removed from the Ta tube and a small piece was ground using a mortar and pestle. A small amount of high vacuum grease was applied to a glass slide and the powder sample of LiGa<sub>2</sub>Rh was evenly distributed over the glass slide. The glass slide was then mounted on a round plastic sample puck and analyzed using room temperature powder X-ray diffraction (pXRD). The diffractometer used was a Bruker D8 Advance Eco using Cu K<sub>α</sub> radiation ( $\lambda = 1.5406 \text{ \AA}$ ) also equipped with a LynxEye-XE detector. The pXRD data was collected from  $5 - 110^\circ 2\theta$  over 180 minutes of scan time. Single crystals were easily picked from the sample and were mounted on the tips of Kapton loops. A Bruker Apex II X-ray diffractometer was used to collect room temperature intensity data using Mo radiation K $\alpha_1$  ( $\lambda = 0.71073 \text{ \AA}$ ). All single crystal data were collected over a full sphere of reciprocal space with scans of  $0.5^\circ$  with 10 seconds per frame for the exposure time. The data was acquired using the SMART software and the SAINT program was used to extract the intensities and correct for both polarization and Lorentz effects. XPREP, which is based on face-indexed absorption, was used for numerical absorption corrections.<sup>56</sup> Twinning of the unit cell was tested but was not observed. The crystal structure of LiGa<sub>2</sub>Rh was then solved using direct methods and the refinement was performed by full-matrix least-squares on  $F^2$ .<sup>57</sup> The occupancies for all three sites were tested and each site was determined to be fully occupied with no evidence of vacancies or atomic disorder. The anomalously low thermal displacement parameters for the Li atoms can be attributed to an ambiguity concerning the number of electrons associated with the Li atoms, which have somewhere between 2 and 3 core electrons in this “polar intermetallic” compound. The dramatic sharpness of the specific heat transition of the pure Heusler phase material is a confirmation of the minimal composition variation in the material. The pXRD data for LiGa<sub>2</sub>Rh were used in a Rietveld refinement using the program FullProf Suite and Thompson-Cox-Hastings pseudo-Voigt



peak shapes to confirm that the bulk material and the single crystals had the same composition. The values for the unit cell parameters and atomic positions determined by the single crystal work were used as a starting point in the Rietveld refinement and were found to perfectly describe the bulk material. The crystal structure image of the full-Heusler LiGa<sub>2</sub>Rh was created in the crystal structure visualization program VESTA<sup>58</sup>.

Temperature-dependent magnetic susceptibility, electrical resistivity, and specific heat measurements were performed in order to characterize and confirm the bulk superconductivity. A Quantum Design Physical Property Measurement System (PPMS) Dynacool was used with a vibrating sample magnetometer (VSM) option to measure the temperature-dependent magnetic susceptibility from 1.7 K – 4 K in a 10 Oe applied field for both the zero-field cooled (ZFC) and field-cooled (FC) measurements of pure LiGa<sub>2</sub>Rh. The impure samples of LiGa<sub>2</sub>Rh were measured under similar temperature and applied field conditions. The field-dependent magnetization measurements, used to determine H<sub>c1</sub>, were performed at various temperatures from 1.7 K to 2.3 K (below T<sub>c</sub>) with field sweeps from 0 to 75 Oe. A small polished piece of LiGa<sub>2</sub>Rh (~10 mg) was used for the temperature-dependent specific heat measurement under zero applied field from 1.7 K – 10 K. The impure samples were measured from 1.7 K to 3.5 K to monitor the magnitude of the specific heat transition at T<sub>c</sub> = 2.4 K. The temperature-dependent resistivity was measured in a PPMS Evercool II system from 300 K to 1.8 K. The upper critical field μ<sub>0</sub>H<sub>c2</sub> was estimated from resistivity data taken under applied magnetic fields from 0 – 1.25 kOe near the superconducting transition. For this experiment, 50 μm diameter platinum wire leads were spark-welded to the flat, freshly polished sample surface of LiGa<sub>2</sub>Rh.

The elemental composition of several samples was examined using a FEI Quanta 250FEG scanning electron microscope (SEM) equipped with an Apollo-X SDD energy-dispersive

spectrometer (EDS). The data were analyzed using the EDAX TEAM<sup>TM</sup> software. EDS was used to confirm that the sample of LiGa<sub>2</sub>Rh used for the superconducting characterization measurements was homogenous with an atomic Ga:Rh ratio of 2:1. EDS mapping of impure samples of LiGa<sub>2</sub>Rh suggested that GaRh was a major impurity phase in many of the early samples of LiGa<sub>2</sub>Rh.

The band structures (BS) and density of states (DOS) of LiGa<sub>2</sub>Rh were calculated using the projector augmented wave method<sup>59</sup> and the Vienna ab initio software package (VASP)<sup>60-62</sup>. A standard self-consistent run was performed using a POSCAR file produced from a cif file containing the atomic positions and unit cell parameters of LiGa<sub>2</sub>Rh obtained from the single crystal structure refinement, and an automatically generated 9x9x9 Monkhorst-pack K-points grid. The Python Materials Genomic (pymatgen) package<sup>63</sup> was used to obtain a high symmetry path in the Brillouin zone and KPOINTS file from the output of the self-consistent calculation, which was subsequently used to perform a non-self-consistent run. The pymatgen package was then used to parse and plot the BS and DOS from the output of the non-self-consistent calculation. This method was repeated with spin orbit coupling. The BS and DOS were found to be essentially identical, indicating that SOC is not critical for explaining the superconducting properties of our material, though it appears to be relevant to the potential topological properties.

## **Results – Materials Chemistry - Superconducting Phase Identification and Isolation**

Powder X-ray diffraction (pXRD), temperature-dependent magnetization, and temperature-dependent specific heat measurements were used to track both the purity and the percentage of superconductor in samples of LiGa<sub>2</sub>Rh. **Figure 1a** shows the room temperature pXRD pattern of an early sample of LiGa<sub>2</sub>Rh with a LeBail fit for space group *Fm-3m* (No. 225). There are clearly several other phases present besides LiGa<sub>2</sub>Rh (green bars). The inset of **Figure**

**1a** shows a zoomed-in view of the most intense peak around 42.5 degrees  $2\theta$ , which is modeled well by  $K_{\alpha 1}$  and  $K_{\alpha 2}$  splitting of the (220) reflection. Even with a clearly impure sample based on pXRD data, a very large diamagnetic response is observed below 2.4 K (**Figure 1b inset**). The temperature-dependent specific heat measurement gives a much better approximate percentage of superconductor in the sample, where, at least for conventional superconductors, the ratio  $\Delta C/\gamma T_c$  must be within experimental error of 1.43 as a minimum value (discussed previously).<sup>47</sup> The main panel of **Figure 1b** shows a plot of  $C_p/T$  vs  $T$  for the impure sample of LiGa<sub>2</sub>Rh measured from 1.7 K – 3.5 K. The anomaly at 2.4 K, while significant, demonstrates a normalized specific heat jump  $\Delta C/\gamma T_c$  of only 0.46, reflecting the fact that the sample is not pure. In contrast, the pure sample of LiGa<sub>2</sub>Rh gave  $\Delta C/\gamma T_c = 1.48$  (discussed later). Based on the ratio of these two normalized specific heat jumps, the impure sample was determined to be ~31 % superconductor. Even with such a large impurity percentage, around 70%, the normalized magnetic moment vs. temperature data for the powdered sample (**Figure 1b, inset**) shows a relatively strong diamagnetic signal ( $-8.0 \times 10^{-5}$  emu/mg) below  $T_c = 2.4$  K, clearly demonstrating the difficulties in using magnetic susceptibility (and resistivity) to identify and isolate a compound superconductor when other potentially superconducting phases are present.

Another sample of LiGa<sub>2</sub>Rh was prepared by arc-melting and the pXRD pattern is shown in the main panel of **Figure 2a**. This sample appears on casual inspection to be single phase LiGa<sub>2</sub>Rh since there are only reflections where there should be peaks for space group  $Fm-3m$  (green vertical bars) and  $a_0 = 5.997(1)$  Å, the cell of the full Heusler phase. On closer inspection it is seen, however, that the reflection at 42.5 degrees is slightly broader (**Figure 2a, inset**) than that shown in the inset of **Figure 1a**, which was considered initially to be a result of preparing the sample by arc-melting, resulting in compositional inhomogeneities. Arc-melting is a less well-

controlled process for obtaining materials that include volatile elemental constituents than sealing the pure elements in a tantalum tube and heating in a furnace under more well-controlled conditions, as was done for the sample in **Figure 1a**. Even though the arc-melted sample appears to be single phase by pXRD, the specific heat measurement (**Figure 2b, main panel**) shows that this sample contains only ~26 % superconductor, which is even less than in the sample shown in **Figure 1b**. However, the moment vs. temperature at 1.7 K shows a diamagnetic signal of  $-1.6 \times 10^{-4}$  emu/mg for this “chunk” sample, which is twice as strong as that seen in the sample that had 5 % more superconductor in the sample (**Figure 1b, inset**), due to different demagnetization factors for the two samples. It should also be noted that it is important to grind the sample into a powder before testing for superconductivity using magnetic susceptibility. This helps to break up the regions that are surrounded by a superconducting phase that cause shielding, which helps to give more reliable diamagnetic signals. This illustrates even more dramatically the importance of specific heat measurements in the process of superconductor identification and isolation.

To further reinforce our conclusions based on diffraction and specific heat analysis, energy-dispersive X-ray spectroscopy (EDS) was used to analyze a pure full Heusler superconducting sample and an impure sample, the latter of which was shown to be inhomogeneous with significant amounts of an impurity phase with a Ga:Rh ratio of 1:1 and minor amounts of impurities with other Ga:Rh ratios. **Figure 3** shows an EDS elemental distribution map composed of Ga-K and Rh-L signals for an impure sample of LiGa<sub>2</sub>Rh. A mosaic-like structure confirms the sample inhomogeneity- the blue color represents the Ga-rich and grey the Ga-poor regions. (Li was not analyzed, since this element contains only 3 electrons and hence is undetectable by the EDS technique.) Regions of Ga-Rh impurities (grey) are surrounded by the superconducting compound (blue), illustrating the “hollow superconducting bubbles” that cause

diamagnetic susceptibility, as well as resistivity, characterization of new superconductors to sometimes be deceptive. When GaRh ( $Pm-3m$ , No. 221) was then added into the LeBail fit for the sample that was only 26 % superconductor, the fit to the diffraction data became significantly better, as shown in **Figure 4 (top)**. In addition, the reflection at 42.5 degrees  $2\theta$  is much better described by two peaks rather than by just one. Even though this sample had a stronger diamagnetic signal than the sample that more clearly showed impurity peaks by pXRD in **Figure 1a**, it turned out to be a sample that was also far from pure. However, the level of purity was hard to distinguish initially without the specific heat measurement since all the reflections of GaRh (light green bars) overlap with reflections for LiGa<sub>2</sub>Rh (dark green bars) except for one reflection at 25 degrees  $2\theta$  that is specific only to LiGa<sub>2</sub>Rh. When a pure sample of the full-Heusler LiGa<sub>2</sub>Rh was finally synthesized, the pXRD pattern was compared with that of the sample with LiGa<sub>2</sub>Rh and the impurity GaRh as shown in **Figure 4 (bottom)**. The reflection at 25 degrees is relatively more intense in the pure LiGa<sub>2</sub>Rh sample (blue line), than in the sample containing GaRh as well (pink line). In addition, the reflection at 42.5 degrees  $2\theta$  is broad enough to be described by two peaks for the impure sample as described previously, but the pure LiGa<sub>2</sub>Rh sample clearly displays  $K_{\alpha 1}$  and  $K_{\alpha 2}$  splitting (blue line) with a much narrower peak (**Figure 4, bottom inset**). In addition, EDS elemental mapping on the pure sample of LiGa<sub>2</sub>Rh confirms that the sample is homogenous with a Ga:Rh ratio of 2:1 (data not shown).

Single crystal X-ray diffraction was used to analyze the crystal structure of the pure sample of the full-Heusler LiGa<sub>2</sub>Rh, which was shown to crystallize in the Cu<sub>2</sub>MnAl structure-type ( $Fm-3m$ , No. 225) with lattice parameter  $a = 5.9997(8)$  Å. A summary of the single crystal refinement is shown in **Table 1** and the atomic coordinates from the structure refinement are shown in **Table 2**. The crystal structure reported here is consistent with what has been inferred previously

from the unit cell parameters determined by powder X-ray diffraction.<sup>6</sup> The inset of **Figure 5** shows the crystal structure of the full-Heusler LiGa<sub>2</sub>Rh with Rh on the *4a* position (0, 0, 0), Li on the *4b* at (½, ½, ½), and Ga on the *8c* position at (¼, ¼, ¼), respectively. In contrast, the previously reported full-Heusler superconductors have the transition metal<sup>7,31,32,34,46</sup> on the *8c* position, rather than a main group element as is found here.

### **Results –Characterization of the Superconducting Properties**

The temperature-dependent magnetic susceptibility,  $\chi = \delta M / \delta H$ , where  $M$  is the magnetization and  $H$  is the applied magnetic field, was measured for pure LiGa<sub>2</sub>Rh with  $H = 10$  Oe in both zero-field cooled (ZFC) and field-cooled (FC) measurements (**Figure 6, main panel**). Both datasets were corrected for a demagnetization factor,  $N = 0.368$ , which was estimated from the field-dependent magnetization data (discussed next). The superconducting critical temperature,  $T_c$ , was taken to be 2.4 K where the diamagnetic signal first manifests. At 1.7 K, the diamagnetic signal for the ZFC measurement saturates to reach within error of  $4\pi\chi_V(1-N) = -1$ , which indicates a full Meissner state. The diamagnetic signal of the FC measurement only reaches  $4\pi\chi_V(1-N) = -0.13$  as is typically seen for polycrystalline samples of superconductors. The inset of **Figure 6** shows the moment vs temperature data normalized per milligram of sample. Even though this sample of LiGa<sub>2</sub>Rh is phase pure, the diamagnetic signal at 1.7 K is only negligibly larger than for the impure sample of LiGa<sub>2</sub>Rh presented in the inset of **Figure 2b**. This is due to different demagnetization factors for the two samples.

The field-dependent magnetization for LiGa<sub>2</sub>Rh was measured to determine both the demagnetization factor and estimate the value of the lower critical field,  $H_{c1}$ . The lower left inset of **Figure 7** shows  $M(H)$  curves measured for different temperatures from 1.7 K to 2.3 K in applied field sweeps from 0 – 75 Oe. A full Meissner state should produce a linear magnetization response

in an applied field. At 1.7 K, the linear region of the  $M(H)$  curve was fitted to a line,  $M_{\text{fit}}$ . The slope,  $b$ , of the  $M_{\text{fit}}$  line was then used to determine the demagnetization factor  $N$ , a factor based on the sample shape and orientation in a magnetic field, using the equation  $-b = \frac{1}{4\pi(1-N)}$ . The  $M_{\text{fit}}$  line was then used to construct the  $M_V - M_{\text{fit}}$  vs. applied field curves in the right inset of **Figure 7**. The magnetic field corresponding to the first deviation from a linear response (black dashed line) for each temperature, or the lower critical field,  $H_{c1}^*$ , (uncorrected for the demagnetization factor) was then plotted in the main panel of **Figure 7**. The  $H_{c1}^*$  vs  $T$  data were fitted with the equation,

$$H_{c1}^*(T) = H_{c1}^*(0) \left[ 1 - \left( \frac{T}{T_c} \right)^2 \right]$$

from the Ginzburg-Landau (GL) theory where  $H_{c1}^*(0)$  is the zero temperature lower critical field and  $T_c = 2.4$  K for the superconductor LiGa<sub>2</sub>Rh. The data is fitted well and results in  $H_{c1}^*$  at 0 K of 37.4(5) Oe and, once corrected for the demagnetization factor of 0.368,  $H_{c1}(0) = 59$  Oe.

Even though the pXRD data for LiGa<sub>2</sub>Rh (**Figure 5**) was fit very well by a model for a full-Heusler phase (space group  $Fm-3m$ ) and the temperature-dependent magnetic susceptibility data (**Figure 6**) showed a full Meissner state at 1.7 K, the only way to truly confirm a bulk superconducting transition in LiGa<sub>2</sub>Rh is with a specific heat measurement. The main panel of **Figure 8** shows a plot of  $C_p/T$  vs  $T$  for LiGa<sub>2</sub>Rh measured from 1.7 K – 3.5 K under zero applied magnetic field. The sharp anomaly corresponding to the thermodynamic transition in LiGa<sub>2</sub>Rh from the normal state to the superconducting state is clearly observed at 2.4 K, consistent with the  $T_c$  from the magnetic susceptibility measurement. An equal-area construction (light blue shading) is shown with a vertical line at 2.4 K and a linear approximation of the  $C_p/T$  data just above and just below  $T_c$  (black solid lines). To determine the Sommerfeld parameter,  $\gamma$ , a plot of  $C_p/T$  vs  $T^2$  was made (**Figure 8, inset**) and fitted to the following equation:

$$\frac{c_p}{T} = \gamma + \beta T^2,$$

where  $\beta T^3$  and  $\gamma T$  are the phonon contribution and the electronic specific heat coefficient to the specific heat, respectively. Using  $\gamma = 4.73(1) \text{ mJ mol}^{-1} \text{ K}^{-2}$ , the normalized specific heat jump  $\Delta C/\gamma T_c = 1.48$ , which is only slightly above 1.43<sup>47</sup> and confirms bulk superconductivity in the full-Heusler LiGa<sub>2</sub>Rh. With a simple Debye model for the phonon contribution,  $\beta = 0.235(2) \text{ mJ mol}^{-1} \text{ K}^{-4}$  from the linear fit can be related to the Debye temperature  $\Theta_D$  through the following equation:

$$\Theta_D = \left( \frac{12\pi^4}{5\beta} nR \right)^{\frac{1}{3}}$$

where  $R = 8.314 \text{ J mol}^{-1} \text{ K}^{-1}$  as the ideal gas constant and  $n = 4$  for the full-Heusler LiGa<sub>2</sub>Rh. The Debye temperature was calculated to be 320(1) K. With the Debye temperature and  $T_c$ , the electron-phonon coupling constant,  $\lambda_{ep}$ , can be calculated using the inverted McMillan<sup>64</sup> equation:

$$\lambda_{ep} = \frac{1.04 + \mu^* \ln\left(\frac{\Theta_D}{1.45T_c}\right)}{(1 - 0.62\mu^*) \ln\left(\frac{\Theta_D}{1.45T_c}\right) - 1.04}$$

where  $\mu^*$  is typically assumed to be 0.13 for numerous intermetallic superconductors. With  $\Theta_D = 320(1) \text{ K}$  and  $T_c = 2.4 \text{ K}$ , we calculated  $\lambda_{ep} = 0.52$ , which suggests that the full-Heusler LiGa<sub>2</sub>Rh is a weak-coupling superconductor. The density of states at the Fermi energy  $N(E_F)$  can be related to  $\lambda_{ep}$  and  $\gamma$  by the following equation:

$$N(E_F) = \frac{3\gamma}{\pi^2 k_B^2 (1 + \lambda_{ep})}$$

where  $k_B$  is the Boltzmann constant.  $N(E_F)$  was calculated to be 1.32 states  $\text{eV}^{-1}$  per formula unit of LiGa<sub>2</sub>Rh.

The temperature-dependent electrical resistivity was measured for LiGa<sub>2</sub>Rh from 300 K to 1.7 K and is shown in the left inset of **Figure 9**. The low residual resistivity ratio (RRR= ( $R_{300}$



$\kappa)/(R_{4.2K})$ ) suggests the presence of disorder in the characterized sample, although the extremely sharp specific heat anomaly at  $T_c$  and the excellent structure refinement indicate that there is no significant compositional inhomogeneity in the material. In addition, the sample of LiGa<sub>2</sub>Rh is a polycrystalline sample and carriers are scattered on grain boundaries. It also may be that the need to solder the contacts on the material, elevating the temperature of the sample in air, is an issue in the qualitative measurement of the resistivity. The temperature-dependent resistivity was then measured from 3.0 K to 1.7 K in applied fields ranging from 0 to 1.25 kOe (**Figure 9**, *right inset*). Under zero applied field, the resistivity drops to zero at  $T_c = 2.5$  K, which is slightly higher than for the magnetic susceptibility and specific heat measurements. With  $H = 1.25$  kOe, the  $T_c$  was suppressed to 1.8 K. The  $T_c$  for each magnetic field was taken as 50 % of the superconducting transition (dashed line) and the results were plotted in the main panel of **Figure 9**. The resulting  $\mu_0 H_{c2}$  vs T data for LiGa<sub>2</sub>Rh were then fitted to a line with a slope equal to  $d\mu_0 H_{c2}/dT = -0.184(1)$  T/K. For a type-II BCS superconductor, the zero temperature upper critical field can be calculated using the Werthamer-Helfand-Hohenberg (WHH) equation,<sup>65</sup>

$$\mu_0 H_{c2}(0) = -AT_c \left. \frac{d\mu_0 H_{c2}}{dT} \right|_{T=T_c}$$

where A is the purity factor as 0.693 for the dirty limit or 0.73 for the clean limit. Taking  $T_c = 2.4$  K, we calculate  $\mu_0 H_{c2}(0) = 0.31$  T for the dirty limit and 0.32 T for the clean limit, respectively. Using the Ginzburg-Landau formula,<sup>47</sup>

$$H_{c2}(0) = \frac{\Phi_0}{2\pi\xi_{GL}^2}$$

where  $\Phi_0 = hc/2e$  is the quantum flux, the superconducting coherence length was calculated to be  $\xi_{GL} = 326$  Å. The superconducting penetration depth can be estimated from the relationship

$$H_{c1} = \frac{\Phi_0}{4\pi\lambda_{GL}^2} \ln \frac{\lambda_{GL}}{\xi_{GL}}$$

to give  $\lambda_{GL} = 2342 \text{ \AA}$ . The ratio of  $\lambda_{GL}$  and  $\xi_{GL}$  gives  $\kappa_{GL} = 7.2$  [ $\kappa_{GL} = \lambda_{GL} / \xi_{GL}$ ], which can then be used in the following equation

$$H_{c1}H_{c2} = H_c^2 \ln \kappa_{GL}$$

with the upper and lower critical magnetic fields to determine the thermodynamic critical field,  $\mu_0 H_c = 30.5 \text{ mT}$ . The superconducting parameters are summarized in **Table 3** for LiGa<sub>2</sub>Rh.

### Results – Calculated Electronic Structure of the Superconductor

Finally, the electronic structure calculations are presented in **Figure 10**. They are fully consistent with our Heusler compound being a metal, and that the Fermi energy is in the vicinity of several van Hove singularities occurring at critical points in the Brillouin Zone. The band structure shows the electrons on Rh (*4d*) and Ga (*4s* and *4p*) orbitals contribute mostly around the Fermi level. Further, a comparison of the calculated electronic structures in the presence and absence of SOC show that the latter case voids a band crossing at  $\sim 0.3 \text{ eV}$  below the Fermi level near the K point in the Brillouin Zone. Such a band gap opened by spin orbit coupling has been observed in topological materials, which host insulating bulk states but conducting surface states due to the symmetry-protection. The symmetry-based indicator (*Z8*) suggests that LiGa<sub>2</sub>Rh may have a topological surface state that is a Fermi arc connecting the bulk valence and conduction bands at a point between  $\Gamma$  and K in the bulk Brillouin zone.

### Conclusions

We report superconductivity in the full-Heusler LiGa<sub>2</sub>Rh, which crystallizes in the Cu<sub>2</sub>MnAl structure-type. The crystal structure was determined by single crystal X-ray diffraction. To the best of our knowledge, LiGa<sub>2</sub>Rh is the first reported Heusler superconductor containing lithium and the first to have a main group element on the *8c* Wyckoff position instead of a transition

metal.  $\text{LiGa}_2\text{Rh}$  shows a superconducting critical temperature of 2.4 K. Calculated superconducting parameters show that  $\text{LiGa}_2\text{Rh}$  is a weak coupling BCS-type superconductor. Out of the more than 1,000 reported Heusler compounds, only about 30 of them are reported superconductors and  $\text{LiGa}_2\text{Rh}$  adds to this small list. In addition, we show that the specific heat measurement is critical to confirm bulk superconductivity, especially when there can be more than one phase (superconducting or not) present. Finally, electronic structure calculations suggest that this superconductor may display topological surface states below  $T_c$ , and therefore that its detailed electronic character may be of interest for future study.

**Acknowledgments** The materials synthesis was supported by the Department of Energy, Division of Basic Energy Sciences, Grant DE-FG02-98ER45706, and the property characterization was supported by the Gordon and Betty Moore Foundation EPiQS initiative, Grant GBMF-4412. The work at LSU was supported by the Beckman Young Investigator (BYI) program. The research in Poland was supported by the National Science Centre, Grant UMO-2016/22/M/ST5/00435.

### **Author Correspondence**

E.M.C ([carnicom@princeton.edu](mailto:carnicom@princeton.edu))

R.J.C. ([rcava@exchange.princeton.edu](mailto:rcava@exchange.princeton.edu))

**Table 1.** Single crystal data and refinement for LiGa<sub>2</sub>Rh.

Empirical Formula	LiGa <sub>2</sub> Rh
F.W. (g/mol)	249.29
Space group; <i>Z</i>	<i>Fm-3m</i> (No. 225); 4
<i>a</i> (Å)	5.9997(8)
<i>V</i> (Å <sup>3</sup> )	215.97(9)
Extinction Coefficient	0.0098(18)
$\theta$ range (degrees)	5.888-32.878
No. reflections; <i>R</i> <sub>int</sub>	261; 0.0151
No. independent reflections	38
No. parameters	5
<i>R</i> <sub>1</sub> : $\omega R_2$ ( <i>I</i> > 2 $\delta$ ( <i>I</i> ))	0.0185: 0.0510
Goodness of fit	1.416
Diffraction peak and hole (e <sup>-</sup> / Å <sup>3</sup> )	1.262 and -1.012

**Table 2.** Standardized atomic coordinates of LiGa<sub>2</sub>Rh.

Atom	Wyckoff Position	$x$	$y$	$z$	Occupancy	$U_{eq}$
Rh	$4a$	0	0	0	1.000	0.0169(5)
Ga	$8c$	$\frac{1}{4}$	$\frac{1}{4}$	$\frac{1}{4}$	1.000	0.0157(5)
Li	$4b$	$\frac{1}{2}$	$\frac{1}{2}$	$\frac{1}{2}$	1.000	0.004(4)

**Table 3.** Summary of superconductivity parameters of LiGa<sub>2</sub>Rh.

Parameter	Units	LiGa <sub>2</sub> Rh
$T_c$	K	2.4
$\mu_0 H_{c1}(0)$	mT	5.9
$\mu_0 H_{c2}(0)$	T	0.31
$\mu_0 H_c(0)$	mT	30.5
$\xi_{GL}$	Å	326
$\lambda_{GL}$	Å	2342
$\kappa_{GL}$	-	7.2
$\gamma$	mJ mol <sup>-1</sup> K <sup>-2</sup>	4.73
$\Delta C / \gamma T_c$	-	1.48
$\mu_0 H^{\text{Pauli}}$	T	4.4
$\lambda_{ep}$	-	0.52
$N(E_F)$	states eV <sup>-1</sup> per f.u.	1.32
$\Theta_D$	K	320

## Figure Captions

**Figure 1.** a) Room temperature pXRD pattern of an impure sample showing a LeBail fit for  $\text{LiGa}_2\text{Rh}$ . Observed data are shown in red, calculated in black, difference in blue, and the green bars are the expected reflections for space group  $Fm-3m$  (No. 225). Inset: Zoomed view of the most intense reflection at  $\sim 42.5$  degrees showing the peak is fit well. b) Even though the moment vs. temperature (*inset*) shows a strong diamagnetic signal below 2.4 K, the specific heat transition is small (*main panel*) and shows the sample is only  $\sim 31\%$  superconductor.

**Figure 2.** a) Room temperature pXRD pattern of a sample of  $\text{LiGa}_2\text{Rh}$  that appears to be single phase showing a LeBail fit. Observed data are shown in red, calculated in black, difference between observed and calculated in blue, and the green ticks are the expected reflections for space group  $Fm-3m$  (No. 225). Inset: The reflection at  $\sim 42.5$  degrees  $2\theta$  is fitted adequately by one peak. b) The moment vs. temperature shows roughly twice the signal strength as in **Figure 1b** (*inset*), but the specific heat transition (*main panel*) corresponds to only  $\sim 26\%$  superconductor.

**Figure 3.** EDS elemental map of an impure sample of  $\text{LiGa}_2\text{Rh}$ . The bright area is Ga-rich with a Ga:Rh atomic ratio close to 2:1.

**Figure 4.** Top: Room temperature pXRD pattern of  $\text{LiGa}_2\text{Rh}$  with the impurity GaRh showing a much better LeBail fit than in **Figure 2a**. The observed data are shown in red, the calculated pattern in black, the difference plot in blue, the dark green bars are the expected peaks for space group  $Fm-3m$  (No. 225), and the light green bars are for space group  $Pm-3m$  (No. 221). Top inset: The reflection at 42.5 degrees  $2\theta$  is much better modeled by two peaks. Bottom: The room temperature pXRD pattern for an impure sample of  $\text{LiGa}_2\text{Rh}$  (pink) overlaid with a pure sample (blue). Bottom inset: The pure sample clearly shows  $K_{\alpha 1}$  and  $K_{\alpha 2}$  peak splitting while the impure sample is broad for the reflection at 42.5 degrees  $2\theta$ .

**Figure 5.** Rietveld refinement of room temperature pXRD data for LiGa<sub>2</sub>Rh. Red data is observed, the black line is the calculated model, the blue line is the difference, and the green bars are the *Fm-3m* expected reflections. Inset: Crystal structure of the full Heusler compound LiGa<sub>2</sub>Rh from the single crystal refinement. Lithium is shown in yellow, gallium in green, and rhodium in pink.

**Figure 6.** Main panel: Zero-field cooled (ZFC) and field-cooled (FC) temperature-dependent volume magnetic susceptibility,  $\chi_v(T)$ , measured from 1.7 K – 4 K under a 10 Oe applied field. The superconducting critical temperature,  $T_c$ , is 2.4 K. The data were corrected for a demagnetization factor  $N = 0.368$ . Inset: Raw moment vs temperature data normalized per mg of the LiGa<sub>2</sub>Rh sample.

**Figure 7.** Volume magnetization,  $M_v$ , vs applied field,  $H$ , at various temperatures from 1.7 K to 2.3 K with field sweeps from 0 – 75 Oe (*left inset*) and fitted to a line,  $M_{fit}$ . Right inset:  $M_v - M_{fit}$  plotted to estimate the value of  $H_{c1}^*$  in the main panel.

**Figure 8.**  $C_p/T$  vs  $T$  for LiGa<sub>2</sub>Rh measured in zero applied field from 1.7 K – 3.5 K. An equal area construction (blue) was used to determine  $T_c = 2.4$  K and  $\Delta C/\gamma T_c = 1.48$ , which confirms having a bulk superconductor. Inset:  $C_p/T$  vs  $T^2$  measured in  $H = 5000$  Oe in the normal state and fitted to a line to determine  $\gamma$  and  $\beta$ .

**Figure 9.** Main panel: Estimation of the upper critical magnetic field ( $\mu_0 H_{c2}$ ) from the dependence of the superconducting transition on the applied magnetic field (right inset) measured from 0 - 1.25 kOe. The  $T_c$  at each applied field was taken as 50 % of the superconducting transition (black dashed line). Left inset: The temperature-dependent electrical resistivity measured in the normal state from 300 K – 4.2 K under zero applied field.



**Figure 10.** Band structure (BS) and density of states (DOS) of the full Heusler LiGa<sub>2</sub>Rh calculated with spin orbit coupling.

## 5. References

- (1) Heusler, F. Über Magnetische Manganlegierungen. *Verh. Dtsch. Phys. Ges.* **1903**, 5, 219.
- (2) Graf, T.; Felser, C.; Parkin, S. S. P. Simple Rules for the Understanding of Heusler Compounds. *Prog. Solid State Chem.* **2011**, 39, 1–50.  
<https://doi.org/10.1016/j.progsolidstchem.2011.02.001>.
- (3) Ishikawa, M.; Jorda, J. L.; Junod, A. Superconductivity in D- and f-Band Metals. In *Superconductivity in d- and f-band Metals*; Buckel, W., Weber, W., Eds.; Kernforschungszentrum: Karlsruhe, Germany, 1982.
- (4) Pavlyuk, V.; Solokha, P.; Dmytriv, G.; Marciniak, B.; Paul-Boncour, V. The Heusler-Type Alloy MgZn<sub>2</sub>Ce. *Acta Cryst.* **2007**, E63, i161.  
<https://doi.org/10.1107/S1600536807028899>.
- (5) Pavlyuk, V. V.; Dmytriv, G. S.; Chumak, I. V.; Ehrenberg, H.; Pauly, H. The Crystal Structure of the LiAg<sub>2</sub>In Compound. *J. Solid State Chem.* **2005**, 178 (11), 3303–3307.  
<https://doi.org/10.1016/j.jssc.2005.08.005>.
- (6) Czybulka, A.; Petersen, A.; Schuster, H. U. Lithium-Platinmetall-Al(Ga, In)-Legierungen: Neue Farbige Ternäre Intermetallische Phasen. *J. Less Common Met.* **1990**, 161 (2), 303–312. [https://doi.org/10.1016/0022-5088\(90\)90041-H](https://doi.org/10.1016/0022-5088(90)90041-H).
- (7) Klimczuk, T.; Wang, C. H.; Gofryk, K.; Ronning, F.; Winterlik, J.; Fecher, G. H.; Griveau, J. C.; Colineau, E.; Felser, C.; Thompson, J. D.; et al. Superconductivity in the Heusler Family of Intermetallics. *Phys. Rev. B* **2012**, 85, 174505.  
<https://doi.org/10.1103/PhysRevB.85.174505>.
- (8) *Heusler Alloys Properties, Growth, Applications*; Felser, C., Hirohata, A., Eds.; Springer, 2016. <https://doi.org/10.1007/978-3-319-21449-8>.

- (9) Surikov, V. V.; Zhordochkin, V. N.; Astakhova, T. Y. Hyperfine Fields in a New Heusler Alloy Mn<sub>2</sub>CoSn. *Hyperfine Interact.* **1990**, *59*, 469–472.  
<https://doi.org/10.1007/BF02401274>.
- (10) Meinert, M.; Schmalhorst, J. M.; Klewe, C.; Reiss, G.; Arenholz, E.; Böhnert, T.; Nielsch, K. Itinerant and Localized Magnetic Moments in Ferrimagnetic Mn<sub>2</sub>CoGa Thin Films Probed by X-Ray Magnetic Linear Dichroism: Experiment and Ab Initio Theory. *Phys. Rev. B* **2011**, *84*, 132405. <https://doi.org/10.1103/PhysRevB.84.132405>.
- (11) Klaer, P.; Jenkins, C. A.; Alijani, V.; Winterlik, J.; Balke, B.; Felser, C.; Elmers, H. J. Disentangling the Mn Moments on Different Sublattices in the Half-Metallic Ferrimagnet Mn<sub>3</sub>-XCoxGa. *Appl. Phys. Lett.* **2011**, *98*, 212510. <https://doi.org/10.1063/1.3592802>.
- (12) Fischer, J. E.; Karel, J.; Fabbri, S.; Adler, P.; Ouardi, S.; Fecher, G. H.; Albertini, F.; Felser, C. Magnetic Properties and Curie Temperatures of Disordered Heusler Compounds: Co<sub>1+x</sub>Fe<sub>2-x</sub>Si. *Phys. Rev. B* **2016**, *94*, 024418.  
<https://doi.org/10.1103/PhysRevB.94.024418>.
- (13) Ziebeck, K. R. A. Heusler Alloys. In *Alloys and Compounds of d-Elements with Main Group Elements*; Wijn, H. P. J., Ed.; Springer: Heidelberg, 2001; pp 64–314.
- (14) Žutić, I.; Fabian, J.; Sarma, S. D. Spintronics Fundamentals and Applications. *Rev. Mod. Phys.* **2004**, *76*, 323–410. <https://doi.org/10.1103/RevModPhys.76.323>.
- (15) Hirohata, A.; Takanashi, K. Future Perspectives for Spintronic Devices. *J. Phys. D: Appl. Phys.* **2014**, *47*, 193001. <https://doi.org/10.1088/0022-3727/47/19/193001>.
- (16) Nakamura, H.; Kitaoka, Y.; Asayama, K.; Onuki, Y.; Komatsubara, T. Successive Magnetic Transitions in the Heusler Heavy-Fermion System CeInCu<sub>2</sub>. *J. Phys. Soc. Jpn.* **1988**, *57* (7), 2276–2279. <https://doi.org/10.1143/JPSJ.57.2276>.

- (17) Gofryk, K.; Kaczorowski, D.; Czopnik, A. Magnetic and Transport Properties of UPd<sub>2</sub>Sb. *Solid State Commun.* **2005**, *133*, 625–628. <https://doi.org/10.1016/j.ssc.2005.01.007>.
- (18) Lahiouel, R.; Pierre, J.; Siaud, E.; Galera, R. M.; Besnus, M. J.; Kappler, J. P.; Murani, A. P. Kondo Lattice and Heavy Fermions in Heusler Phases: CeInAg<sub>2</sub>-XCux. *Z. Phys. B - Condens. Matter* **1987**, *67* (2), 185–191. <https://doi.org/10.1007/BF01303979>.
- (19) Takabatake, T.; Kawanaka, H.; Fujii, H.; Yamaguchi, Y.; Sakurai, J.; Aoki, Y.; Fujita, T. Structural and Magnetic Phase Transitions in a New Heavy-Fermion Compound UPd<sub>2</sub>In. *J. Phys. Soc. Jpn.* **1989**, *58* (6), 1918–1921. <https://doi.org/10.1143/JPSJ.58.1918>.
- (20) Zhu, T.; Fu, C.; Xie, H.; Liu, Y.; Zhao, X. High Efficiency Half-Heusler Thermoelectric Materials for Energy Harvesting. *Adv. Energy Mater.* **2015**, *5*, 1–13. <https://doi.org/10.1002/aenm.201500588>.
- (21) Hohl, H.; Ramirez, A. P.; Goldmann, C.; Ernst, G.; Wölfing, B.; Bucher, E. Efficient Dopants for ZrNiSn-Based Thermoelectric Materials. *J. Phys. Condens. Matter* **1999**, *11* (7), 1697–1709. <https://doi.org/10.1088/0953-8984/11/7/004>.
- (22) Uher, C.; Yang, J.; Hu, S.; Morelli, D. T.; Meisner, G. P. Transport Properties of Pure and Doped MNiSn (M=Zr, Hf). *Phys. Rev. B* **1999**, *59* (13), 8615–8621. <https://doi.org/10.1103/PhysRevB.59.8615>.
- (23) He, J.; Amsler, M.; Xia, Y.; Naghavi, S. S.; Hegde, V. I.; Hao, S.; Goedecker, S.; Ozoliņš, V.; Wolverton, C. Ultralow Thermal Conductivity in Full Heusler Semiconductors. *Phys. Rev. Lett.* **2016**, *117*, 046602. <https://doi.org/10.1103/PhysRevLett.117.046602>.
- (24) Nishino, Y.; Kato, M.; Asano, S.; Soda, K.; Hayasaki, M.; Mizutani, U. Semiconductorlike Behavior of Electrical Resistivity in Heusler-Type Fe<sub>2</sub>VAl Compound. *Phys. Rev. Lett.* **1997**, *79* (10), 1909–1912.

- <https://doi.org/10.1103/PhysRevLett.79.1909>.
- (25) Buschow, K. H. J.; van Engen, P. G.; Jongebreur, R. Magneto-Optical Properties of Metallic Ferromagnetic Materials. *J. Magn. Magn. Mater.* **1983**, *38*, 1–22.  
[https://doi.org/10.1016/0304-8853\(83\)90097-5](https://doi.org/10.1016/0304-8853(83)90097-5).
- (26) Kämmerer, S.; Thomas, A.; Hütten, A.; Reiss, G. Co<sub>2</sub>MnSi Heusler Alloy as Magnetic Electrodes in Magnetic Tunnel Junctions. *Appl. Phys. Lett.* **2004**, *85*, 79–81.  
<https://doi.org/10.1063/1.1769082>.
- (27) Wurmehl, S.; Fecher, G. H.; Kandpal, H. C.; Ksenofontov, V.; Felser, C.; Lin, H. J.; Morais, J. Geometric, Electronic, and Magnetic Structure of Co<sub>2</sub>FeSi: Curie Temperature and Magnetic Moment Measurements and Calculations. *Phys. Rev. B* **2005**, *72*, 184434.  
<https://doi.org/10.1103/PhysRevB.72.184434>.
- (28) Wurmehl, S.; Fecher, G. H.; Kandpal, H. C.; Ksenofontov, V.; Felser, C.; Lin, H. J. Investigation of Co<sub>2</sub>FeSi: The Heusler Compound with Highest Curie Temperature and Magnetic Moment. *Appl. Phys. Lett.* **2006**, *88*, 032503. <https://doi.org/10.1063/1.2166205>.
- (29) Kainuma, R.; Imano, Y.; Ito, W.; Sutou, Y.; Morito, H.; Okamoto, S.; Kitakami, O.; Oikawa, K.; Fujita, A.; Kanomata, T.; et al. Magnetic-Field-Induced Shape Recovery by Reverse Phase Transformation. *Nature* **2006**, *439* (7079), 957–960.  
<https://doi.org/10.1038/nature04493>.
- (30) Krenke, T.; Duman, E.; Acet, M.; Wassermann, E. F.; Moya, X.; Manosa, L.; Planes, A. Inverse Magnetocaloric Effect in Ferromagnetic Ni-Mn-Sn Alloys. *Nat. Mater.* **2005**, *4* (6), 450–454. <https://doi.org/10.1038/nmat1395>.
- (31) Wernick, J. H.; Hull, G. W.; Geballe, T. H.; Bernardini, J. E.; Waszczak, J. V. Superconductivity in Ternary Heusler Intermetallic Compounds. *Mater. Lett.* **1983**, *2* (2),

- 90–92. [https://doi.org/10.1016/0167-577X\(83\)90043-5](https://doi.org/10.1016/0167-577X(83)90043-5).
- (32) Kierstead, H. A.; Dunlap, B. D.; Malik, S. K.; Umarji, A. M.; Shenoy, and G. K. Coexistence of Ordered Magnetism and Superconductivity in Pd<sub>2</sub>YbSn. *Phys. Rev. B* **1985**, *32* (1), 135–138. <https://doi.org/10.1103/PhysRevB.32.135>.
- (33) Winterlik, J.; Fecher, G. H.; Thomas, A.; Felser, C. Superconductivity in Palladium-Based Heusler Compounds. *Phys. Rev. B* **2009**, *79* (6), 064508. <https://doi.org/10.1103/PhysRevB.79.064508>.
- (34) Waki, S.; Yamaguchi, Y.; Mitsugi, K. Superconductivity of Ni<sub>2</sub>NbX (X=Al, Ga and Sn). *J. Phys. Soc. Jpn.* **1985**, *54* (5), 1673–1676. <https://doi.org/10.1143/JPSJ.54.1673>.
- (35) Shelton, R. N.; Hausermann-Berg, L. S.; Johnson, M. J.; Klavins, P.; Yang, H. D. Coexistence of Superconductivity and Long-Range Magnetic Order in ErPd<sub>2</sub>Sn. *Phys. Rev. B* **1986**, *34* (1), 199–202. <https://doi.org/10.1103/PhysRevB.34.199>.
- (36) Winterlik, J.; Fecher, G. H.; Felser, C.; Jourdan, M.; Grube, K.; Hardy, F.; von Löhneysen, H.; Holman, K. L.; Cava, R. J. Ni-Based Superconductor: Heusler Compound ZrNi<sub>2</sub>Ga. *Phys. Rev. B* **2008**, *78* (18), 184506. <https://doi.org/10.1103/PhysRevB.78.184506>.
- (37) Seaman, C. L.; Dilley, N. R.; de Andrade, M. C.; Herrmann, J.; Maple, M. B.; Fisk, Z. Superconductivity and Magnetism in the Heusler Alloys MPd<sub>2</sub>Pb (M =rare Earth, Th, and U). *Phys. Rev. B* **1996**, *53* (5), 2651–2657. <https://doi.org/10.1103/PhysRevB.53.2651>.
- (38) Malik, S. K.; Umarji, A. M.; Shenoy, G. K. Depression of the Superconducting Transition Temperature of the Heusler Alloy Pd<sub>2</sub>YSn with the Addition of Magnetic Rare-Earth Metals. *Phys. Rev. B* **1985**, *32* (7), 4426–4430. <https://doi.org/10.1103/PhysRevB.32.4426>.

- (39) Johnson, M. J.; Shelton, R. N. Pressure Effects on the Superconductivity of Ternary Rare Earth Palladium Heusler Alloys. *Solid State Commun.* **1984**, *52* (10), 839–842.  
[https://doi.org/10.1016/0038-1098\(84\)90252-7](https://doi.org/10.1016/0038-1098(84)90252-7).
- (40) Xiao, H.; Hu, T.; Liu, W.; Zhu, Y. L.; Li, P. G.; Mu, G.; Su, J.; Li, K.; Mao, Z. Q. Superconductivity in the Half-Heusler Compound TbPdBi. *Phys. Rev. B* **2018**, *97* (22), 224511. <https://doi.org/10.1103/PhysRevB.97.224511>.
- (41) Butch, N. P.; Syers, P.; Kirshenbaum, K.; Hope, A. P.; Paglione, J. Superconductivity in the Topological Semimetal YPtBi. *Phys. Rev. B* **2011**, *84* (22), 220504.  
<https://doi.org/10.1103/PhysRevB.84.220504>.
- (42) Pavlosiuk, O.; Kaczorowski, D.; Wiśniewski, P. Superconductivity and Shubnikov-de Haas Oscillations in the Noncentrosymmetric Half-Heusler Compound YPtBi. *Phys. Rev. B* **2016**, *94*, 035130. <https://doi.org/10.1103/PhysRevB.94.035130>.
- (43) Tafti, F. F.; Fujii, T.; Juneau-Fecteau, A.; René de Cotret, S.; Doiron-Leyraud, N.; Asamitsu, A.; Taillefer, L. Superconductivity in the Noncentrosymmetric Half-Heusler Compound LuPtBi: A Candidate for Topological Superconductivity. *Phys. Rev. B* **2013**, *87* (18), 184504. <https://doi.org/10.1103/PhysRevB.87.184504>.
- (44) Nakajima, Y.; Hu, R.; Kirshenbaum, K.; Hughes, A.; Syers, P.; Wang, X.; Wang, K.; Wang, R.; Saha, S. R.; Pratt, D.; et al. Topological RPdBi Half-Heusler Semimetals: A New Family of Noncentrosymmetric Magnetic Superconductors. *Sci. Adv.* **2015**, *1* (5), e1500242. <https://doi.org/10.1126/sciadv.1500242>.
- (45) Matthias, B. T. Empirical Relation between Superconductivity and the Number of Valence Electrons per Atom. *Phys. Rev.* **1955**, *97* (1), 74–76.  
<https://doi.org/10.1103/PhysRev.97.74>.

- (46) Matthias, B. T. Transition Temperatures of Superconductors. *Phys. Rev.* **1953**, *92* (4), 874–876. <https://doi.org/10.1103/PhysRev.92.874>.
- (47) Tinkham, M. *Introduction to Superconductivity*, 2nd ed.; Dover Publications, Inc.: Mineola, 1996.
- (48) Bortolozo, A. D.; Sant’Anna, O. H.; dos Santos, C. A. M.; Machado, A. J. S. Superconductivity in the Hexagonal-Layered Nanolaminates Ti<sub>2</sub>InC Compound. *Solid State Commun.* **2007**, *144* (10–11), 419–421. <https://doi.org/10.1016/j.ssc.2007.09.028>.
- (49) Bortolozo, A. D.; Serrano, G.; Serquis, A.; Rodrigues, D.; Dos Santos, C. A. M.; Fisk, Z.; Machado, A. J. S. Superconductivity at 7.3 K in Ti<sub>2</sub>InN. *Solid State Commun.* **2010**, *150* (29–30), 1364–1366. <https://doi.org/10.1016/j.ssc.2010.04.036>.
- (50) Bortolozo, A. D.; Sant’Anna, O. H.; da Luz, M. S.; dos Santos, C. A. M.; Pereira, A. S.; Trentin, K. S.; Machado, A. J. S. Superconductivity in the Nb<sub>2</sub>SnC Compound. *Solid State Commun.* **2006**, *139* (2), 57–59. <https://doi.org/10.1016/j.ssc.2006.05.006>.
- (51) Kong, T.; Górnicka, K.; Gołąb, S.; Wiendlocha, B.; Klimczuk, T.; Cava, R. J. A Family of Pb-Based Superconductors with Variable Cubic to Hexagonal Packing. *J. Phys. Soc. Japan* **2018**, *87*, 074711. <https://doi.org/10.7566/JPSJ.87.074711>.
- (52) Jain, A.; Ong, S. P.; Hautier, G.; Chen, W.; Richards, W. D.; Dacek, S.; Cholia, S.; Gunter, D.; Skinner, D.; Ceder, G.; et al. Commentary: The Materials Project: A Materials Genome Approach to Accelerating Materials Innovation. *APL Mater.* **2013**, *1*, 011002. <https://doi.org/10.1063/1.4812323>.
- (53) Van Hove, L. The Occurrence of Singularities in the Elastic Frequency Distribution of a Crystal. *Phys. Rev.* **1953**, *89* (6), 1189–1193. <https://doi.org/10.1103/PhysRev.89.1189>.
- (54) Li, G.; Luican, A.; Lopes Dos Santos, J. M. B.; Castro Neto, A. H.; Reina, A.; Kong, J.;



- Andrei, E. Y. Observation of Van Hove Singularities in Twisted Graphene Layers. *Nat. Phys.* **2010**, *6* (2), 109–113. <https://doi.org/10.1038/nphys1463>.
- (55) Gofron, K.; Campuzano, J. C.; Abrikosov, A. A.; Lindroos, M.; Bansil, A.; Ding, H.; Koelling, D.; Dabrowski, B. Observation of an “Extended” Van Hove Singularity in YBa<sub>2</sub>Cu<sub>4</sub>O<sub>8</sub> by Ultrahigh Energy Resolution Angle-Resolved Photoemission. *Phys. Rev. Lett.* **1994**, *73* (24), 3302–3306. <https://doi.org/10.1103/PhysRevLett.73.3302>.
- (56) SHELXTL. Software Reference Manual, Version 6.10, Bruker Analytical X-Ray System, Inc., Madison, WI, 2000.
- (57) Sheldrick, G. M. A Short History of SHELX. *Acta Crystallogr.* **2008**, *A64* (1), 112–122. <https://doi.org/10.1107/S0108767307043930>.
- (58) Momma, K.; Izumi, F. VESTA 3 for Three-Dimensional Visualization of Crystal, Volumetric and Morphology Data. *J. Appl. Crystallogr.* **2011**, *44* (6), 1272–1276. <https://doi.org/10.1107/S0021889811038970>.
- (59) Kresse, G.; Joubert, D. From Ultrasoft Pseudopotentials to the Projector Augmented-Wave Method. *Phys. Rev. B* **1999**, *59* (3), 1758–1775. <https://doi.org/10.1103/PhysRevB.59.1758>.
- (60) Kresse, G.; Hafner, J. Ab Initio Molecular Dynamics for Liquid Metals. *Phys. Rev. B* **1993**, *47* (1), 558(R). <https://doi.org/10.1103/PhysRevB.47.558>.
- (61) Kresse, G.; Furthmüller, J. Efficiency of Ab-Initio Total Energy Calculations for Metals and Semiconductors Using a Plane-Wave Basis Set. *Comput. Mater. Sci.* **1996**, *6* (1), 15–50. [https://doi.org/10.1016/0927-0256\(96\)00008-0](https://doi.org/10.1016/0927-0256(96)00008-0).
- (62) Kresse, G.; Furthmüller, J. Efficient Iterative Schemes for Ab Initio Total-Energy Calculations Using a Plane-Wave Basis Set. *Phys. Rev. B* **1996**, *54* (16), 11169.

<https://doi.org/10.1103/PhysRevB.54.11169>.

- (63) Ong, S. P.; Richards, W. D.; Jain, A.; Hautier, G.; Kocher, M.; Cholia, S.; Gunter, D.; Chevrier, V. L.; Persson, K. A.; Ceder, G. Python Materials Genomics (Pymatgen): A Robust, Open-Source Python Library for Materials Analysis. *Comput. Mater. Sci.* **2013**, *68*, 314–319. <https://doi.org/10.1016/j.commatsci.2012.10.028>.
- (64) McMillan, W. L. Transition Temperature of Strong-Coupled Superconductors. *Phys. Rev.* **1968**, *167* (2), 331–344. <https://doi.org/10.1103/PhysRev.167.331>.
- (65) Werthamer, N. R.; Helfand, E.; Hohenberg, P. C. Temperature and Purity Dependence of the Superconducting Critical Field,  $H_{c2}$ . III. Electron Spin and Spin-Orbit Effects. *Phys. Rev.* **1966**, *147* (1), 295–302. <https://doi.org/10.1103/PhysRev.147.295>.

# Figures

## Figure 1.

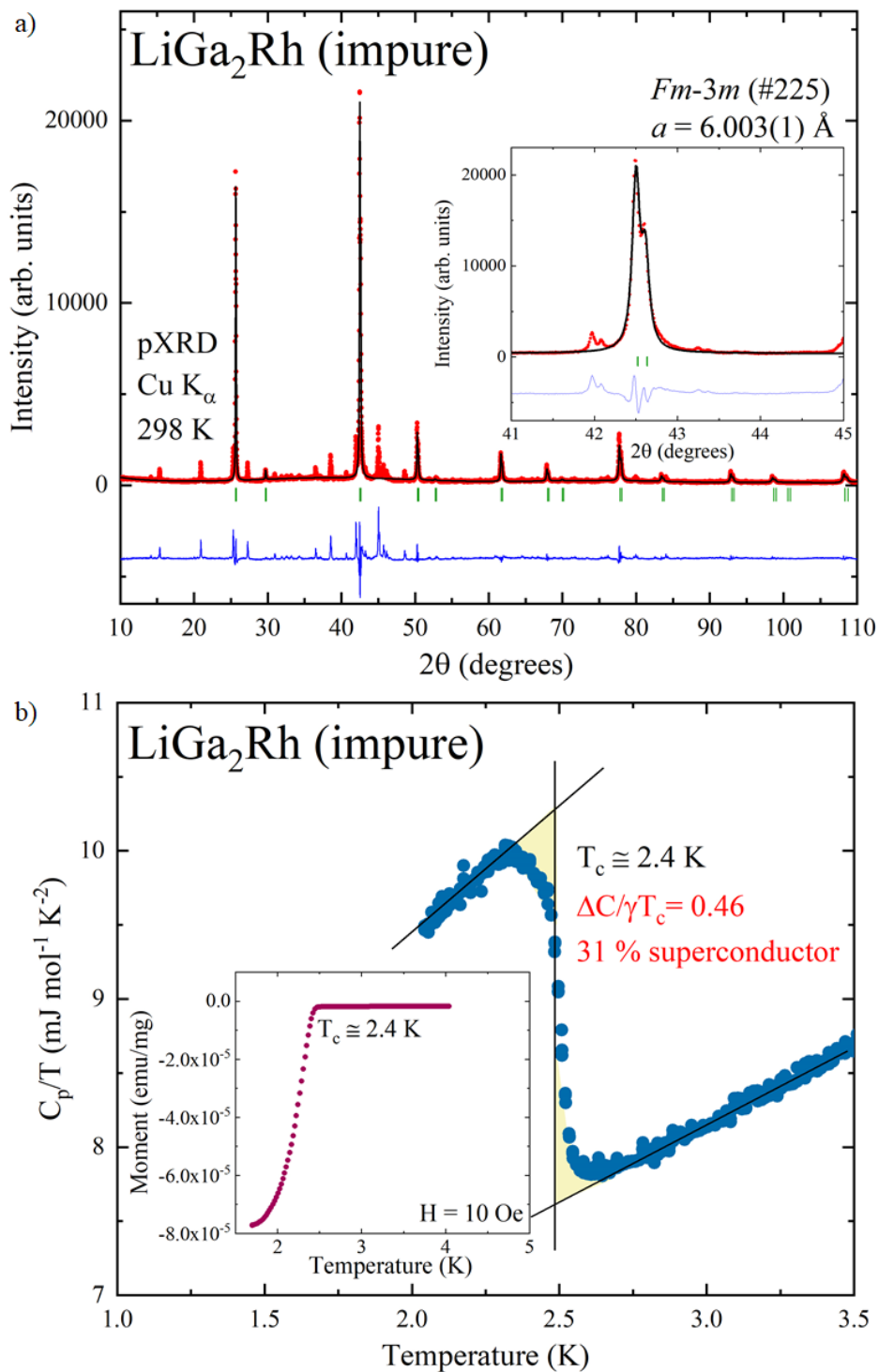


Figure 2.

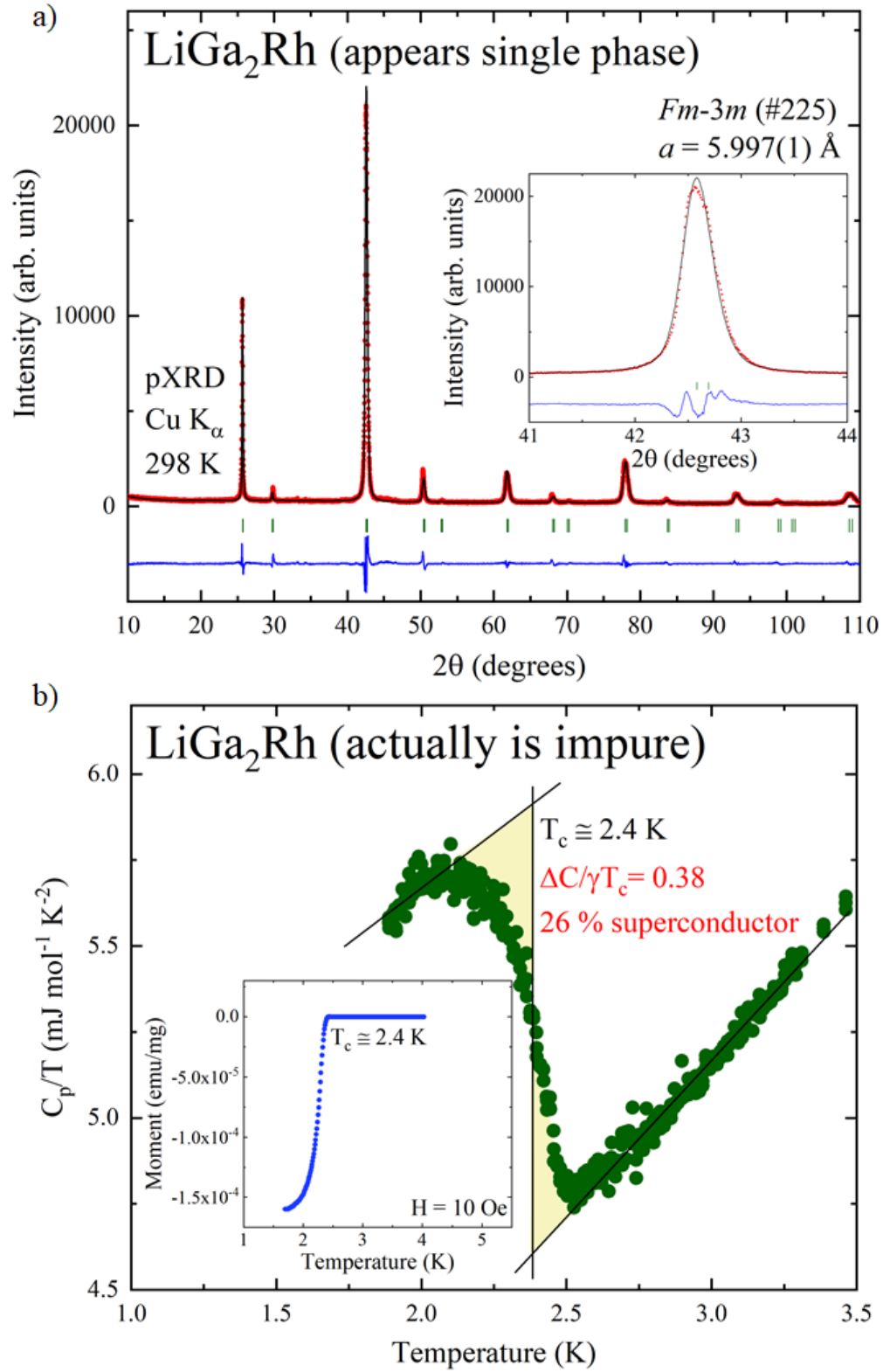


Figure 3.

Impure  $\text{LiGa}_2\text{Rh}$

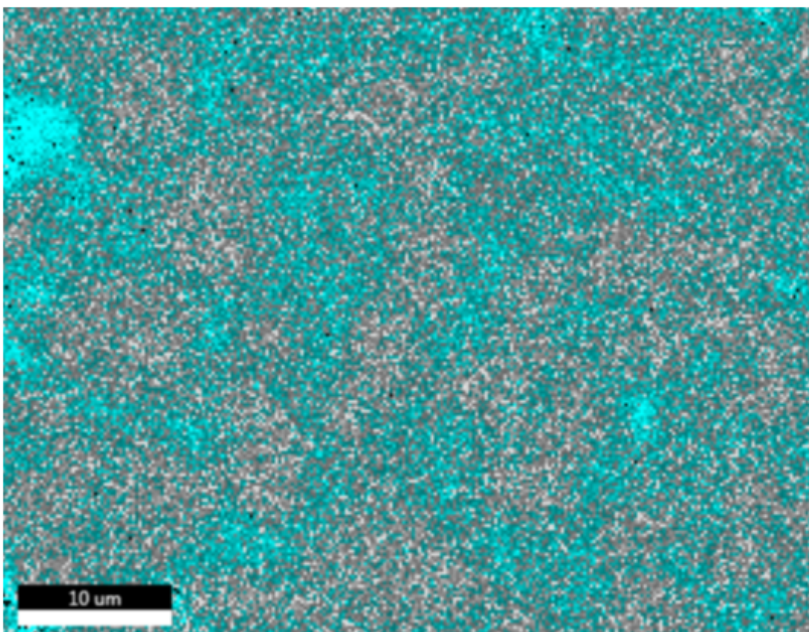


Figure 4.

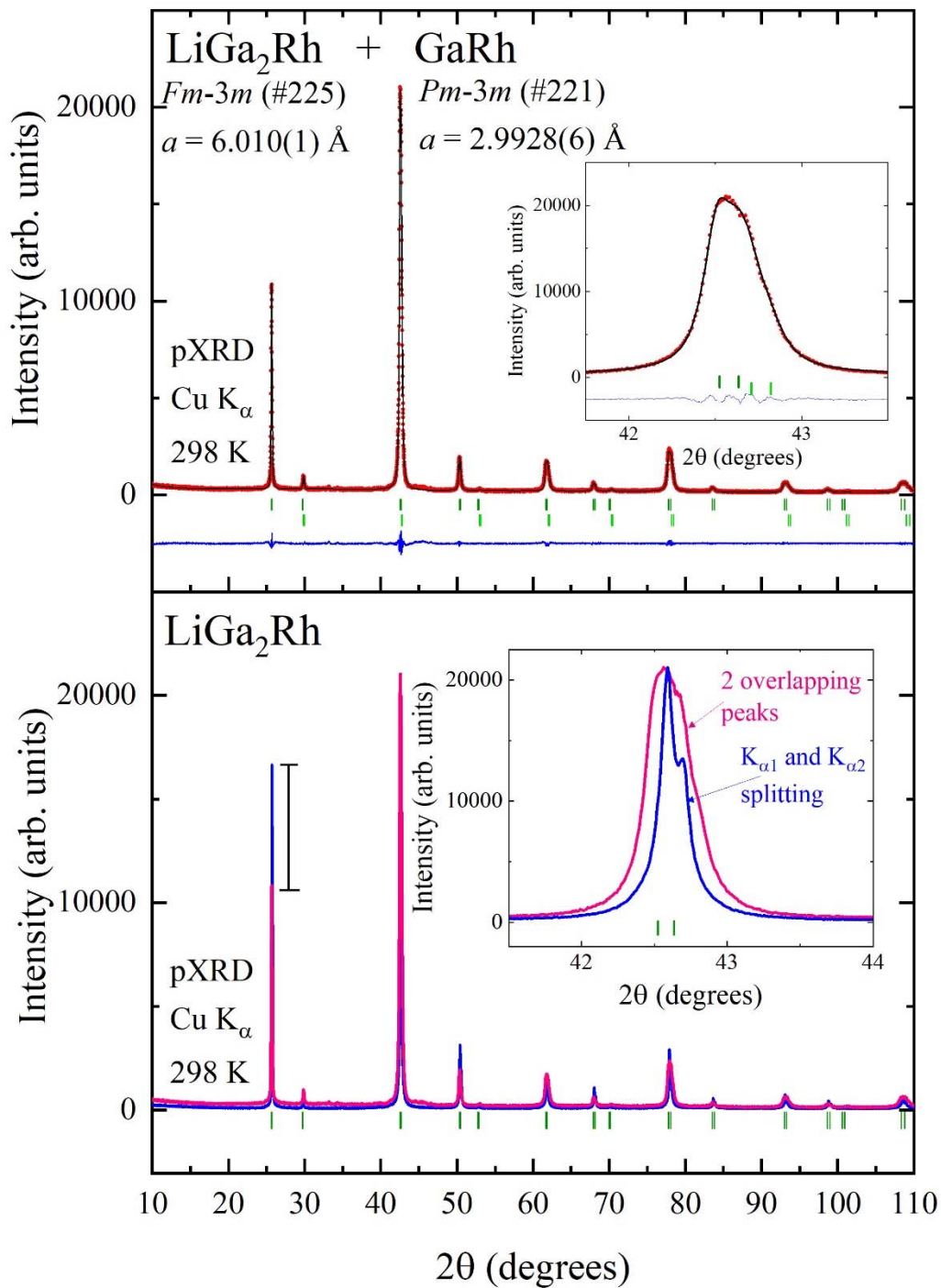


Figure 5.

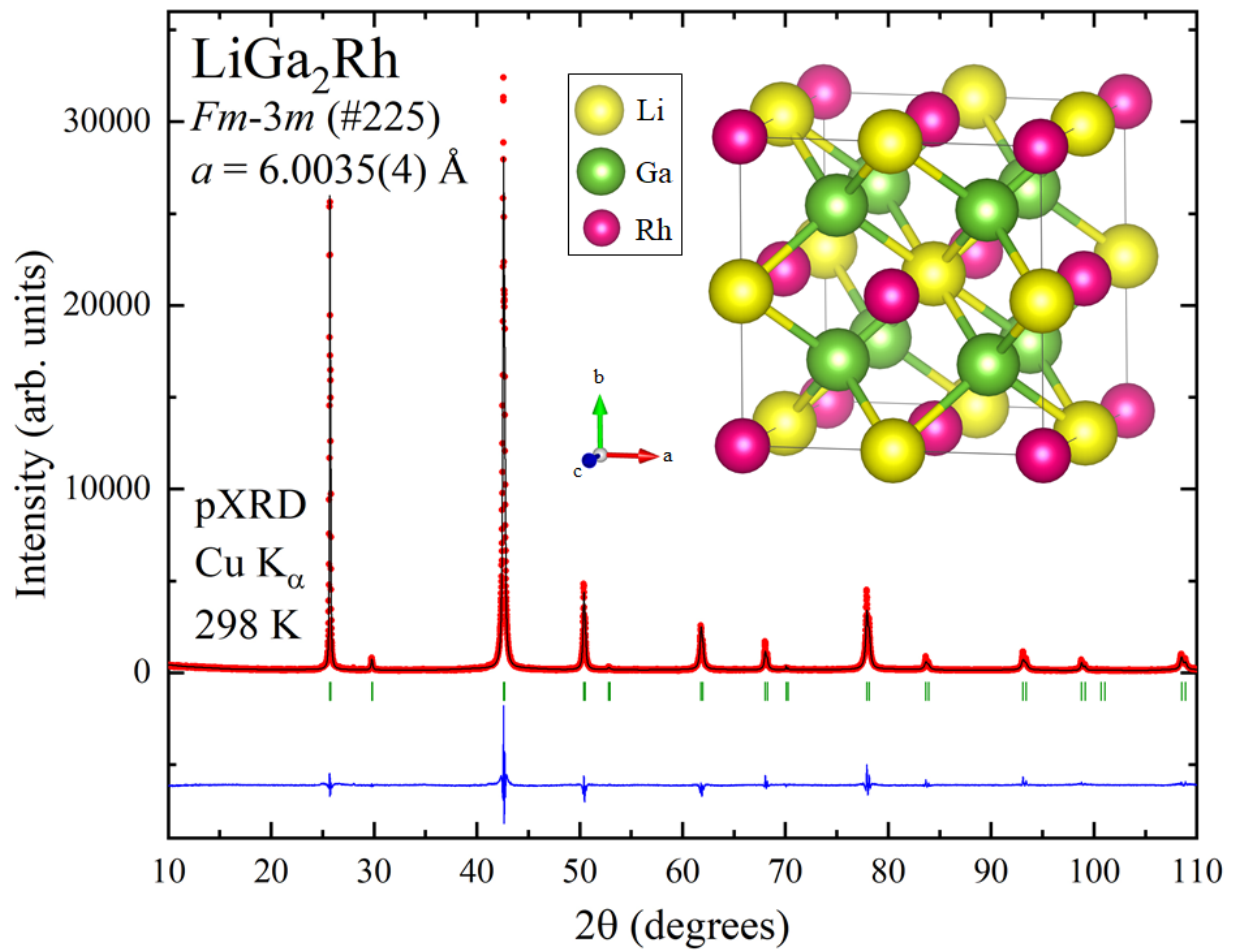


Figure 6.

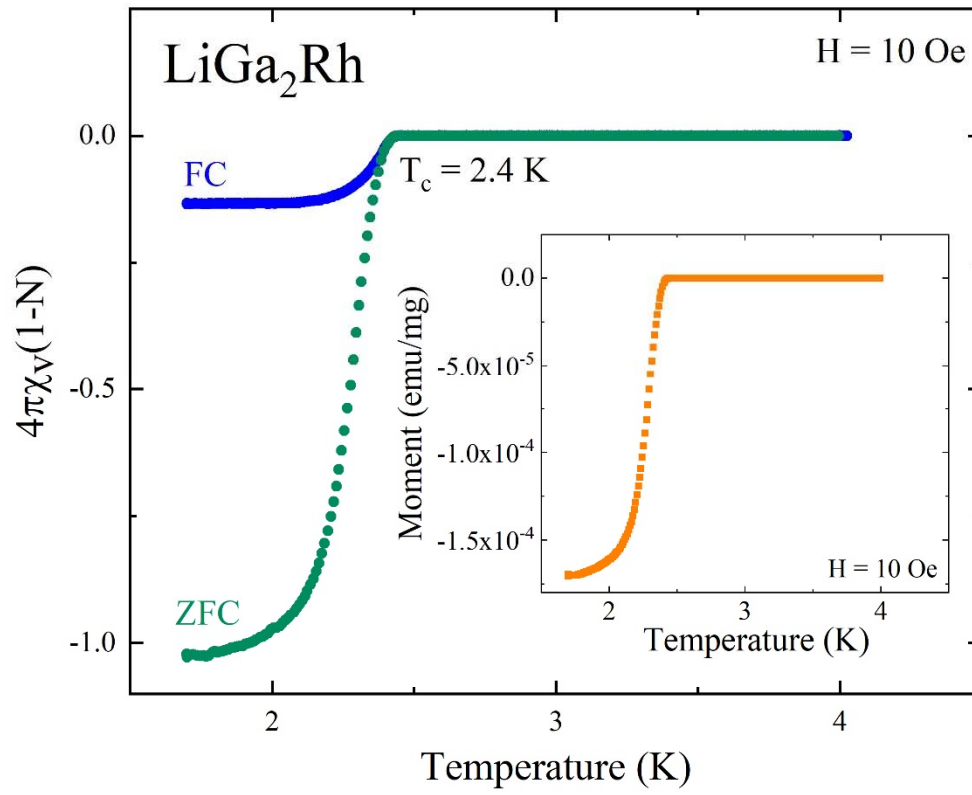




Figure 7.

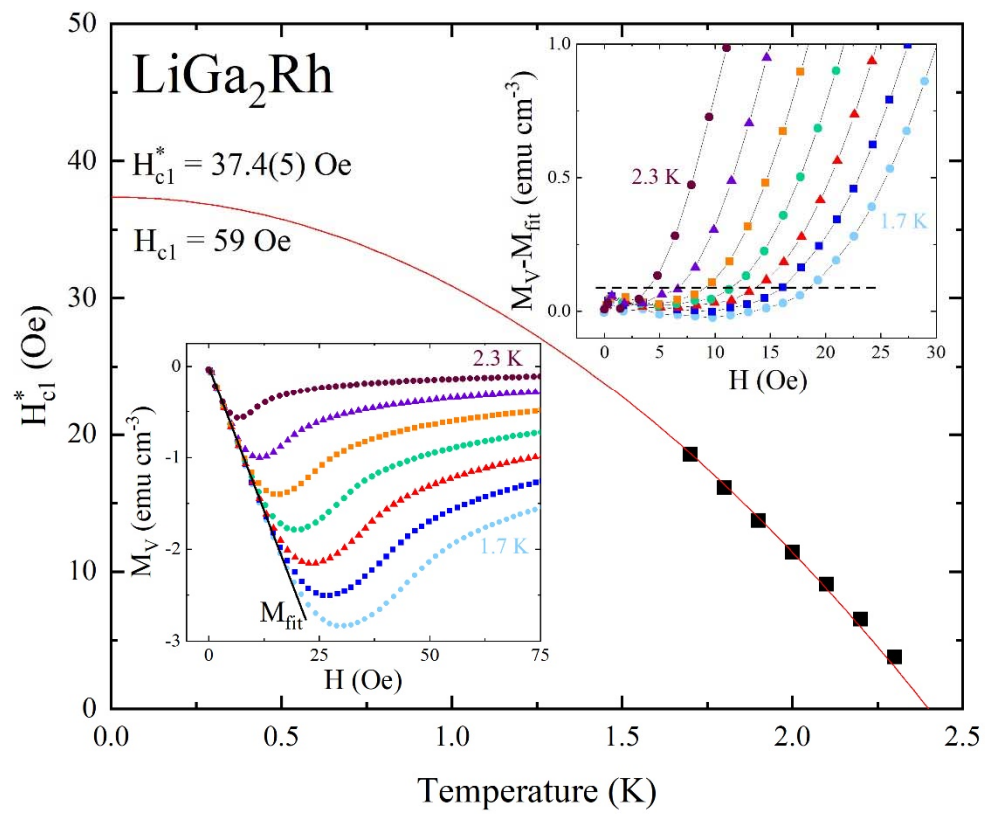


Figure 8.

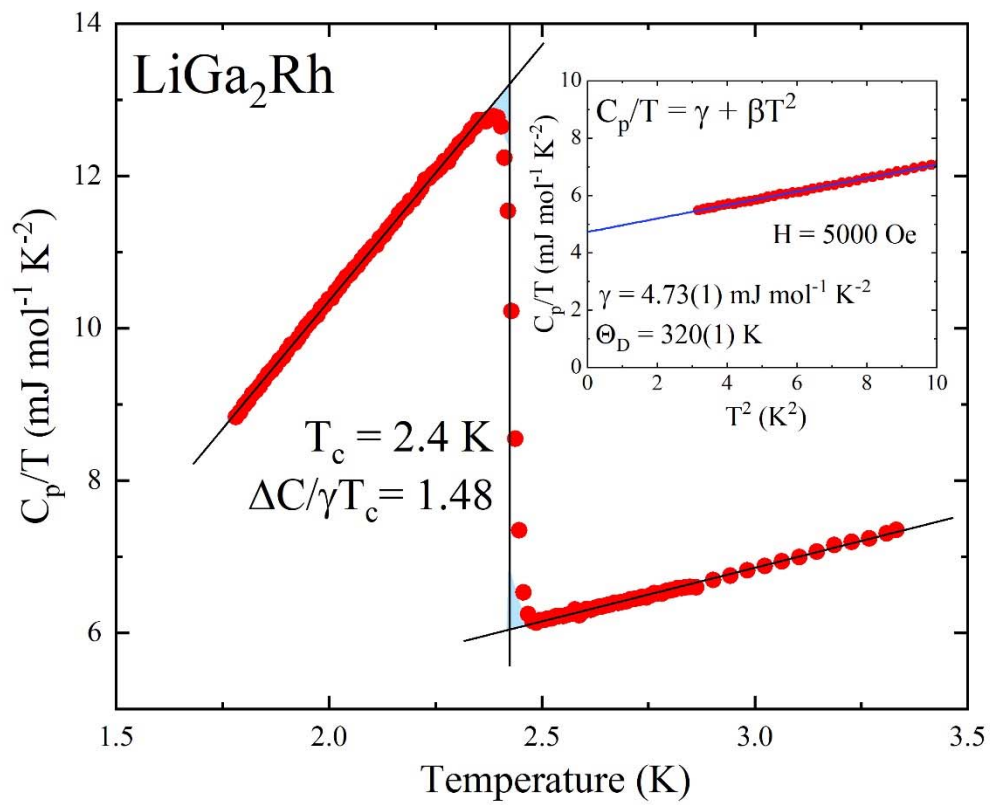




Figure 10.

